

## Article

# Modeling of Durum Wheat Yield Based on Sentinel-2 Imagery

Chris Cavalaris , Sofia Megoudi, Maria Maxouri, Konstantinos Anatolitis, Marios Sifakis, Efi Levizou   
and Aris Kyparissis \* 

Department of Agricultural Crop Production and Rural Environment, School of Agricultural Sciences, University of Thessaly, Fytokou Str., 38446 Volos, Greece; chkaval@uth.gr (C.C.); sofiamegg5@gmail.com (S.M.); mar.maxouri@gmail.com (M.M.); k.anatolitis95@gmail.com (K.A.); msifakis33@gmail.com (M.S.); elevizou@uth.gr (E.L.)

\* Correspondence: akypar@uth.gr

**Abstract:** In this study, a modelling approach for the estimation/prediction of wheat yield based on Sentinel-2 data is presented. Model development was accomplished through a two-step process: firstly, the capacity of Sentinel-2 vegetation indices (VIs) to follow plant ecophysiological parameters was established through measurements in a pilot field and secondly, the results of the first step were extended/evaluated in 31 fields, during two growing periods, to increase the applicability range and robustness of the models. Modelling results were examined against yield data collected by a combine harvester equipped with a yield-monitoring system. Normalized Difference Vegetation Index (NDVI) and Enhanced Vegetation Index (EVI) were examined as plant signals and combined with Normalized Difference Water Index (NDWI) and/or Normalized Multiband Drought Index (NMDI) during the growth period or before sowing, as water and soil signals, respectively. The best performing model involved the EVI integral for the 20 April–31 May period as a plant signal and NMDI on 29 April and before sowing as water and soil signals, respectively ( $R^2 = 0.629$ , RMSE = 538). However, model versions with a single date and maximum seasonal VIs values as a plant signal, performed almost equally well. Since the maximum seasonal VIs values occurred during the last ten days of April, these model versions are suitable for yield prediction.

**Keywords:** durum wheat; yield modelling; Sentinel-2; NDVI; EVI; NDWI; NMDI



**Citation:** Cavalaris, C.; Megoudi, S.; Maxouri, M.; Anatolitis, K.; Sifakis, M.; Levizou, E.; Kyparissis, A. Modeling of Durum Wheat Yield Based on Sentinel-2 Imagery. *Agronomy* **2021**, *11*, 1486. <https://doi.org/10.3390/agronomy11081486>

Academic Editor: Jiftah Ben-Asher

Received: 29 June 2021  
Accepted: 23 July 2021  
Published: 27 July 2021

**Publisher's Note:** MDPI stays neutral with regard to jurisdictional claims in published maps and institutional affiliations.



**Copyright:** © 2021 by the authors. Licensee MDPI, Basel, Switzerland. This article is an open access article distributed under the terms and conditions of the Creative Commons Attribution (CC BY) license (<https://creativecommons.org/licenses/by/4.0/>).

## 1. Introduction

Durum wheat (*Triticum turgidum* L. var. durum) is a crop used for a variety of food products, mainly pasta. Almost 60% of the world durum wheat cultivated area, about 7.8 million hectares, is located at the Mediterranean basin [1]. Nevertheless, pasta consumption in the Mediterranean countries is higher than the local production, so food industries depend on imports from other durum-wheat-producing territories, mainly North America. Furthermore, the final production relies mainly on weather conditions, especially during the grain-filling stage [2]. The variability of the Mediterranean climate, exacerbated by the on-going climate change, causes great year-to-year fluctuations in durum wheat yields. This fact causes risks and uncertainty in the industry, grain marketing agencies, policymakers, and other involved entities, concerning the planning of their exports and imports. Early-season prediction of durum wheat yields is of vital importance for assisting the whole food production chain. Farmers as well, can adjust the farm inputs, such as fertilizers and irrigation, to meet the site-specific needs of the crop by implementing precision agriculture techniques, while the harvesting sector can plan its logistics by managing the harvester fleet and anticipating transport and storage requirements.

So far, yield prediction for winter wheat relies on either estimates and information gathered from experts or on outputs from a variety of crop simulation models, such as CERES [3], WOFOST [4], CROPSYST [5], or SAFY [6]. Even though models like the CERES-wheat have been used quite successfully for more than 30 years [7], the main drawback is

that they require numerous data for weather, climate, soil, genotypes, and management practices that are often difficult to obtain. Moreover, these models are poor predictors when within-field spatial variability is considerable [8]. More recently, remotely sensed data have been used complementarily to improve the accuracy of crop models [9–12]. Remotely sensed data retrieved from satellite observations can provide quantitative and temporal information over large areas, through the use of vegetation indices (VIs), such as the normalized difference vegetation index (NDVI) [13], the enhanced vegetation index (EVI) [14], and the normalized difference red edge index (NDRE) [15]. Such VIs are closely related to vegetation biophysical parameters, such as the canopy leaf area index (LAI) or the fraction of absorbed photosynthetically active radiation (fAPAR) [16,17], which are commonly used in vegetation productivity modeling.

Even though spatial variability in crop productivity is highly associated with soil properties, water, and nutrient availability [2,18], remote-sensed data from the crop canopy have been proved a valuable tool for yield predictions, as they directly depict most of these effects on crop development [19]. Among the different approaches used for yield prediction, the empirical methods based on the straightforward application of a statistical regression between a VI and yield are the most common, because of their simplicity and limited data requirements [20–26]. The main drawback of this approach is that the relationships between VIs and yield are often limited to the regions for which they were calibrated and are not globally applicable [24,27]. Bhattacharya et al. [28] attributed the site-dependent nature of the spectral yield models on the saturation of some VIs (e.g., NDVI) at high levels of LAI, and the insensitivity of VIs to soil moisture variation, especially at moderate to full canopy cover conditions. Nevertheless, Becker-Reshef et al. [9] managed to develop a winter wheat single regression model where the yield was positively and linearly correlated to the seasonal maximum NDVI from MODIS data. The generalized model was calibrated and applied at the state level in Kansas and was proven directly transferable and applicable at the national level in Ukraine.

Multispectral instruments onboard several satellites (e.g., LANDSAT, MODIS, and SPOT) have provided plenty of data used for vegetation monitoring [9,25,29–35]. However, their utility is often compromised by their low spatial or temporal resolution or their limited public availability. MODIS offers a spatial resolution for the NDVI-associated bands at 250 m pixel size. This corresponds to 6.25 ha and is considered too large for the average farm size in the Mediterranean basin, which may be as small as 6.8 ha, as in the case of Greece (Eurostat—farm structure statistics). LANDSAT provides higher spatial resolution (30 m pixel size) but with a 16-day revisit cycle, which is rather low to produce accurate and continuous VI time-series, especially during periods of rapid phenological/physiological changes [9]. The more recent SPOT-7 satellite offers high spatial resolution at 6 m and is capable of providing revisits on a daily basis, but its services are available on-demand and are not freely accessible.

Lately, the European Space Agency (ESA) launched a pair of satellites namely Sentinel-2 (A and B) equipped with a MultiSpectral Instrument (MSI), that deliver data at five-day intervals, with multiple spectral bands at 10 m, 20 m, and 60 m spatial resolution [36]. These frequently captured, high resolution, open data seem particularly suitable for effective yield prediction at the sub-field level and for precision agricultural applications. Sentinel-2A was launched in 2015 and Sentinel-2B in 2017, and due to the short period of their operation, research information for specific crops and vegetation parameters are still quite limited. Xie et al. [37] used Sentinel-2 data to estimate winter wheat LAI, leaf, and canopy chlorophyll content and compared the results with in situ measurements. In a comparative study, Prey and Schmidhalter [26] demonstrated that VIs extracted from Sentinel-2 MSI sensor clearly outperformed the Landsat-8, Worldview-2, and RapidEye sensors in the estimation of VIs related to wheat grain yield, grain N uptake, and grain N concentration.

The aim of the present study was to develop a simple yield prediction model based on high spatial resolution Sentinel-2 data, suitable for the small-size fields of the Mediterranean basin. Model development was accomplished through a two-step process: firstly, the

capacity of Sentinel-2 VIs to follow plant ecophysiological parameters was established through field measurements in a pilot field and the most suitable plant, water, and soil signals for yield prediction were determined and secondly, the results of the first step were extended/evaluated in 31 wheat fields with different varieties, management practices, and soil composition, during two growing periods, to extent the applicability range and robustness of the model. In all steps modelling results were examined against yield data collected by a harvesting machine equipped with a yield-monitoring system.

## 2. Materials and Methods

### 2.1. Study Sites

The study sites were located in Thessaly plain, central Greece and the monitoring involved the 2017–2018 and 2018–2019 growing periods (Figure 1). One field ( $39^{\circ}34'52.13''$  N,  $22^{\circ}35'46.22''$  E) from the 2018–2019 period was selected as a pilot for field measurements and model development. The pilot field was chosen because of the high variability of its soil electrical conductivity, as shown in Figure 2d. Another 31 fields, 19 from the 2017–2018 growing period and 12 from the 2018–2019, were used for model evaluation. The criteria for selecting the fields were (i) the availability of yield map data and (ii) an adequate size, scheme, and orientation capable of providing a sufficient number of Sentinel-2,  $10 \times 10$  m resolution pixels. All the fields were cultivated with durum wheat of different varieties (Iridae, Meridiano, Normano, Simeto, and Svevo) and belonged to numerous farmers who followed their own cultivation practices. That way, the model could be evaluated in different conditions and also, it could be ensured that it applied regardless of the cropping practices.

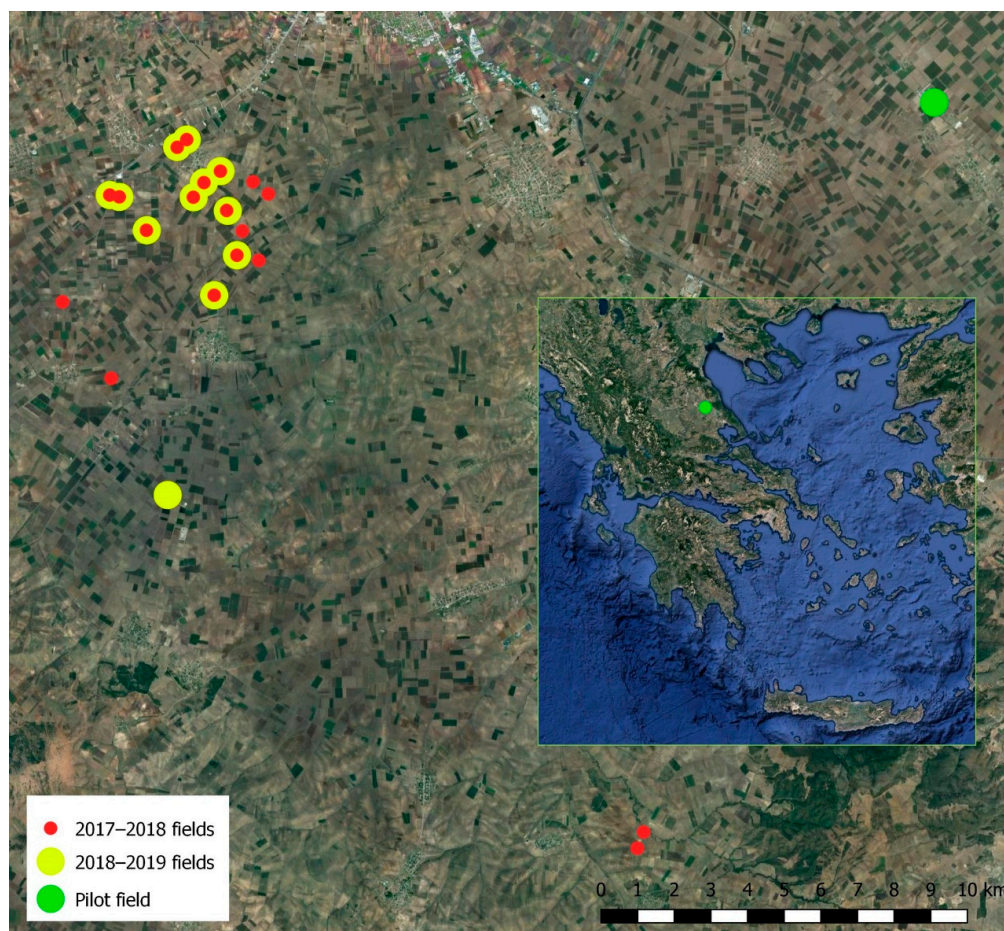


**Figure 1.** Satellite image of the Thessaly plain, Greece (inset), with the studied fields indicated.

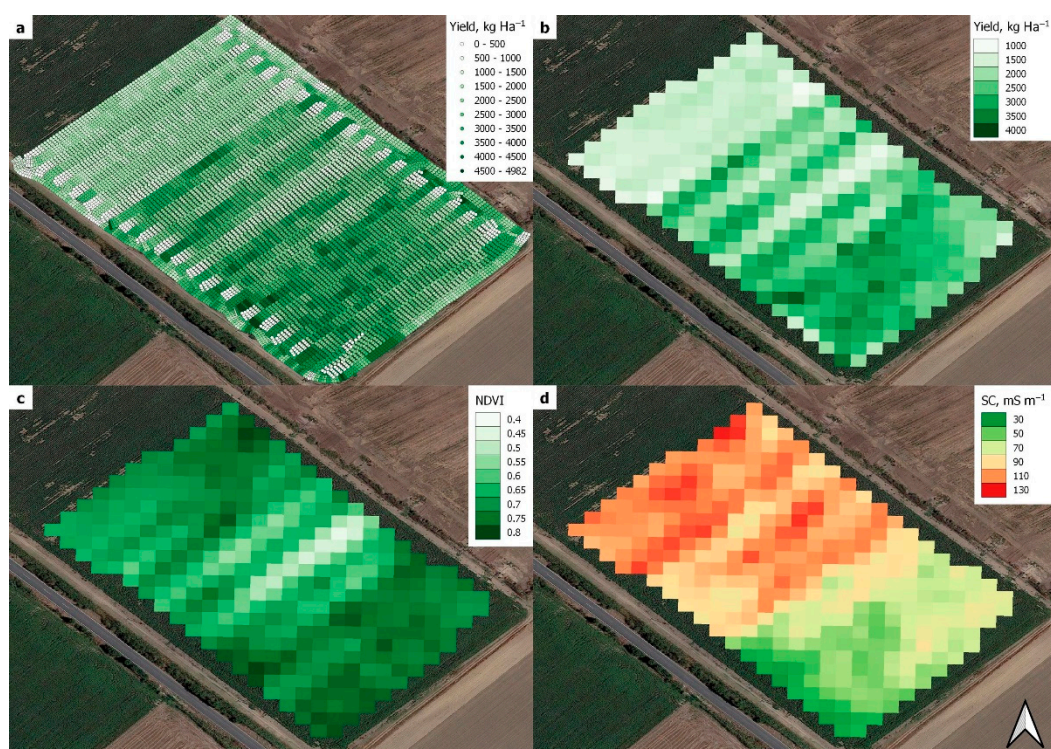


**Figure 2.** Raw yield data as provided by the harvesting machine (a) and after noise removal, rasterization, resampling, and collocation with Sentinel-2 pixels (b); Sentinel-2 NDVI on 29 April 2019 (c); soil ECa map spatial resolution after, rasterization, resampling, and collocation with Sentinel-2 pixels (d).

The 4.5 ha pilot field was cultivated with Svevo variety at a seed rate of  $230 \text{ kg ha}^{-1}$ . Six  $30 \times 30 \text{ m}$  plots were accurately determined by GPS (Garmin, eTrex, Schaffhausen, Switzerland) to collocate with Sentinel-2 pixels (9 Sentinel-2 pixels per plot). All ecophysiological measurements were performed in these plots and compared with the corresponding Sentinel-2 data.

## 2.2. Field Measurements

### 2.2.1. Leaf Area Index

Leaf area index was measured with an AccuPAR LP-80 PAR/LAI Ceptometer (Decagon Devices, Inc., Pullman, WA, USA) following Norman and Jarvis model [38] of radiation transmission and scattering. Three LAI measurements were performed per plot, with 10 below and one above canopy PAR measurements per LAI measurement. PAR sampling points were randomly selected at 3 m intervals across three transects in each plot. For the below canopy measurements, the Ceptometer was placed at an angle of approximately  $45^\circ$  in relation to cultivation lines. All measurements were performed during clear-sky days and around solar noon.

### 2.2.2. Water Potential

Water potential ( $\Psi$ ) was measured using a Scholander-type pressure chamber (SKPM 1400, Skye Instruments Ltd., Liandrindrod, UK). Randomly selected whole plants across plots were wrapped in aluminum foil and sealed in plastic bags for 10 min and then cut and measured immediately with the pressure chamber.

### 2.2.3. Soil Electrical Conductivity

The soil apparent electrical conductivity (ECa) was measured using an EM38 instrument (Geonics Ltd., Mississauga, ON, Canada). The whole field was scanned at 22 March 2018 by walking the field in parallel lines, about 15 m apart, with the instrument handheld

5 cm above the ground. The instrument records ECa at time intervals of 1s providing geo-tagged data used to create a point vector map. The vector map was initially interpolated into a raster with a resolution of 1x1m using the ordinary kriging process in the SAGA v.7.9.0 free open-source GIS (SAGA User Group Association, 2020, Kent, UK). Accordingly, the raster map was resampled and collocated to the 10 × 10 m pixels of Sentinel-2. using the QGIS v.3.16 open-source Geographic Information System.

#### 2.2.4. Canopy Reflectance

Canopy reflectance was measured in situ with a portable JAZ spectroradiometer (OceanOptics, Dunedin, FL, USA), with spectral range from 350 to 1000 nm and spectral resolution approximately 0.3 nm. Measurements were taken with a 5 m length optical fiber in combination with a home-made supporting system at a height approximately 1 m from top of the canopy. The spectroradiometer was calibrated against a Spectralon® white reflectance panel (Labsphere, Inc., North Sutton, NH, USA) before the measurements' onset and every 15 min, to track solar angle changes. All measurements were performed during clear-sky days and around solar noon time. At each plot 30 measurements were taken at 3–4 m intervals, by walking at three random lines forming a Z scheme.

#### 2.2.5. Yield Measurement

At the end of the growing periods (June) the fields were harvested with a John Deere S660i combine harvester equipped with a yield mapping system providing, through the associated MyJD software, a yield map in a point vector format at a spatial resolution of 1.75 by approximately 2.5 m (depending on the travelling speed) (Figure 2a). The initial maps were further processed with the open-source Yield Editor software (v.2.0.7) [39] for the removal of outliers (due to start point, end point grain flow delays, swath width overlaps, rapid speed changes, etc.). Accordingly, the yield maps were interpolated to rasters by the IDW process of QGIS and finally, resampled at 10 × 10 m pixel size (Figure 2b) corresponding to the Sentinel-2 image pixels (Figure 2c).

#### 2.3. Satellite Data

A total of 61 cloud-free Sentinel-2 (A and B) images from October 2017 to June 2018 and October 2018 to June 2019 were downloaded from ESA's Copernicus Open Access Hub [40] (<https://scihub.copernicus.eu/>). The MultiSpectral Instruments (MSI), onboard the Sentinel-2 satellites, provide information at 13 spectral bands (443–2190 nm), at a variable spatial resolution from 10, 20, or 60 m pixel size and with a 5-day revisit time. In the present study, Level 2A (radiometrically and atmospherically corrected) bottom of atmosphere (BOA) reflectance products provided by ESA, were used. All images were resampled at 10 m pixel size using the SNAP-ESA Sentinels Application Platform v.6.0.4 [41] (<http://step.esa.int>) free open-source software. After data extraction for the pixels of the studied sites (221 pixels for the pilot field used for model development and 7436 pixels for the evaluation fields), time-series were constructed for the following vegetation indices:

$$\text{Normalized difference vegetation index, NDVI} = \frac{R_{842} - R_{665}}{R_{842} + R_{665}} \quad (1)$$

$$\text{Enhanced vegetation index, EVI} = 2.5 \frac{R_{842} - R_{665}}{R_{842} + 6R_{665} - 7.5R_{490} + 1} \quad (2)$$

$$\text{Normalized difference water index, NDWI} = \frac{R_{842} - R_{2190}}{R_{842} + R_{2190}} \quad (3)$$

$$\text{Normalized multiband drought index, NMDI} = \frac{R_{842} - (R_{1610} - R_{2190})}{R_{842} + (R_{1610} - R_{2190})} \quad (4)$$

where  $R_x$ , reflectance at wavelength  $x$ , with  $x$  denoting the center wavelength of the corresponding Sentinel-2 band.

Accordingly, the 221 + 7436 pixels  $\times$  4 VIs time series were linearly interpolated producing complete daily datasets for the corresponding growing periods (October to June). Linear interpolation and the absence of any smoothing process on the VI time series were chosen to keep processing as simple as possible, for the whole methodology to be easily applied in the modelling process. The interpolated daily datasets were subsequently used for the calculation of VI integrals for varying time intervals across the growing periods. Additionally, several soil indices were calculated for a single date before sowing (bare ground) and their formulations are shown in Table 1.

**Table 1.** Correlation coefficients (R) between reflectance of Sentinel-2 bands as well as several indices with soil ECa and final yield.

S2 Band	Central $\lambda$ nm	R Soil ECa	R Yield	Index	Abbreviation	Formula	R Soil ECa	R Yield
B1	443	−0.069	0.073	Normalized difference Water index	NDWI	$(B8 - B12)/(B8 + B12)$	0.511	−0.435
B2	490	0.016	−0.074	Color index	CI	$(B4 - B3)/(B4 + B3)$	0.188	−0.257
B3	560	0.150	−0.186	Salinity index	SI	$B4 \times B8/B3$	0.099	−0.230
B4	665	0.191	−0.243	Brightness index	BI	$\sqrt{(B4^2 + B3^2)/2}$	0.177	−0.224
B5	705	0.172	−0.282	Brightness index 2	BI2	$\sqrt{(B4^2 + B3^2 + B8^2)/3}$	0.118	−0.204
B6	740	0.121	−0.269	Redness index	RI	$B4^2/B3^3$	−0.029	0.024
B7	783	0.057	−0.223	Soil-adjusted vegetation index	SAVI	$1.5 \times (B8 - B4)/(B8 + B4 + 0.5)$	−0.472	0.195
B8	842	0.055	−0.180		BSI	$\frac{(B11 + B4) - (B8 - B2)}{(B11 + B4) + (B8 - B2)}$	−0.261	0.203
B8A	865	0.005	−0.194	Normalized difference Vegetation index	NDVI	$(B8 - B4)/(B8 + B4)$	−0.504	0.290
B9	945	−0.133	0.003	Normalized multiband Drought index	NMDI	$\frac{B8 - (B11 - B12)}{B8 + (B11 - B12)}$	−0.637	0.526
B11	1610	−0.330	0.074					
B12	2190	−0.518	0.258					

#### 2.4. Statistics

The relationships between VIs and field-measured parameters were examined through correlation analyses, while the performance of estimation models was evaluated using linear and multilinear regression analyses, from which coefficient of determination ( $R^2$ ) and root-mean-square error (RMSE) were derived ( $p$ -value < 0.05). All analyses were performed using JASP software v.0.14 [42].

### 3. Results

#### 3.1. Sentinel VIs and Field Measurements

Even though it is generally established that satellite VIs are good estimators of plant ecophysiological parameters, species- and site-specific relationships have to be well documented. To that purpose several Sentinel-2 VIs were examined against field-measured ecophysiological parameters in the pilot field.

##### 3.1.1. Sensor Intercomparison

Canopy reflectance was measured with two different remote sensors—the MultiSpectral Instrument (MSI) onboard the Sentinel-2 satellite and the hyperspectral JAZ canopy spectroradiometer. Even though these two sensors have differences in spectral, spatial, and radiometric characteristics, their measurements may be used for the calculation of several widely used vegetation indices. In this study the JAZ spectroradiometer was used as a reference, since it has a super-fine spectral analysis (0.3 nm), it is calibrated before each measurement against a standard reflectance panel, and it is operated very close to the canopy avoiding any atmospheric disturbance effects. Accordingly, Sentinel-2 performance was evaluated on the basis of vegetation indices intercomparisons. For that purpose, the detailed spectral data of the JAZ spectroradiometer were averaged over the spectral range of the Sentinel-2 bands used in vegetation indices calculations. For each 30  $\times$  30 m plot the JAZ measurements were averaged and compared to the average values of the corresponding nine Sentinel-2 pixels.

Vegetation indices NDVI and EVI from Sentinel-2 correlated very well with JAZ indices, showing high correlation coefficients, as well as slopes and intercepts close to 1 and 0, respectively (Figure 3). The large error bars for JAZ data may be considered rather reasonable due to its small measurement area (approximately  $15 \times 15$  cm with the optical fiber at 1 m height above the canopy) resulting in detailed monitoring of the occurring variability, which is smoothed in the  $10 \times 10$  m Sentinel-2 data.

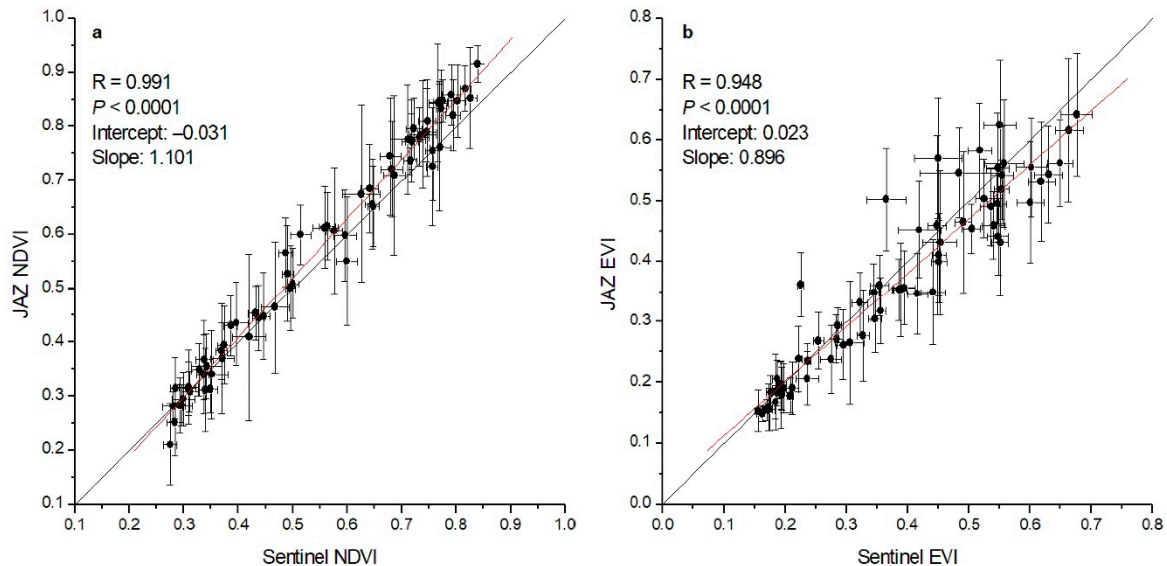


**Figure 3.** Relationships between JAZ and Sentinel-2 NDVI (a) and EVI (b). Data concern dates with both Sentinel-2 acquisitions and JAZ measurements. Each point corresponds to the mean from 10 JAZ measurements performed in one plot at one date and the mean from the corresponding 9 Sentinel-2 pixels  $\pm$  standard deviation.

### 3.1.2. Leaf Area Index and Satellite VIs

Leaf area index was measured in the pilot field from February to May 2019. As shown in Figure 4, the seasonal course of the crop is well depicted in LAI, with low values during winter, gradually increasing until the April flowering period, followed by a rather steep decrease during the May seed-ripening period. This pattern was also followed by the satellite VIs (Figure 5), resulting in very good correlations between field-measured LAI and VIs (Figure 6).

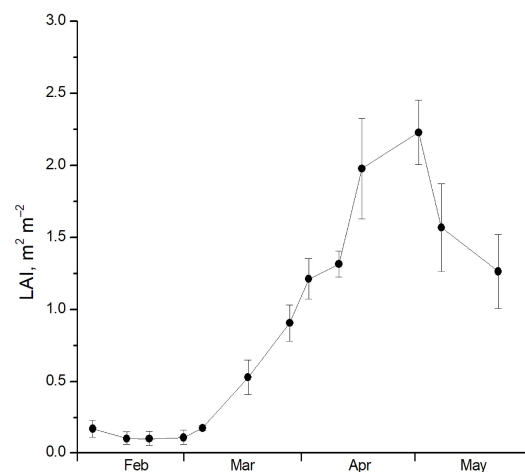


**Figure 4.** Seasonal fluctuation of leaf area index. Data are means from six plots (10 measurements per plot)  $\pm$  standard deviation.

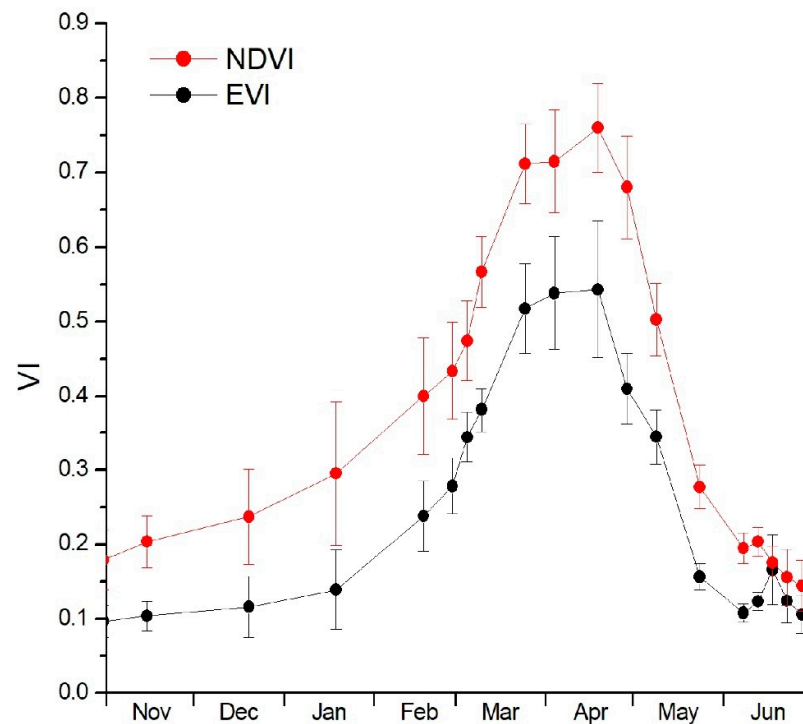


**Figure 5.** Seasonal fluctuation of Sentinel-2 vegetation indices (NDVI and EVI). Data are means from six plots (9 pixels per plot)  $\pm$  standard deviation.

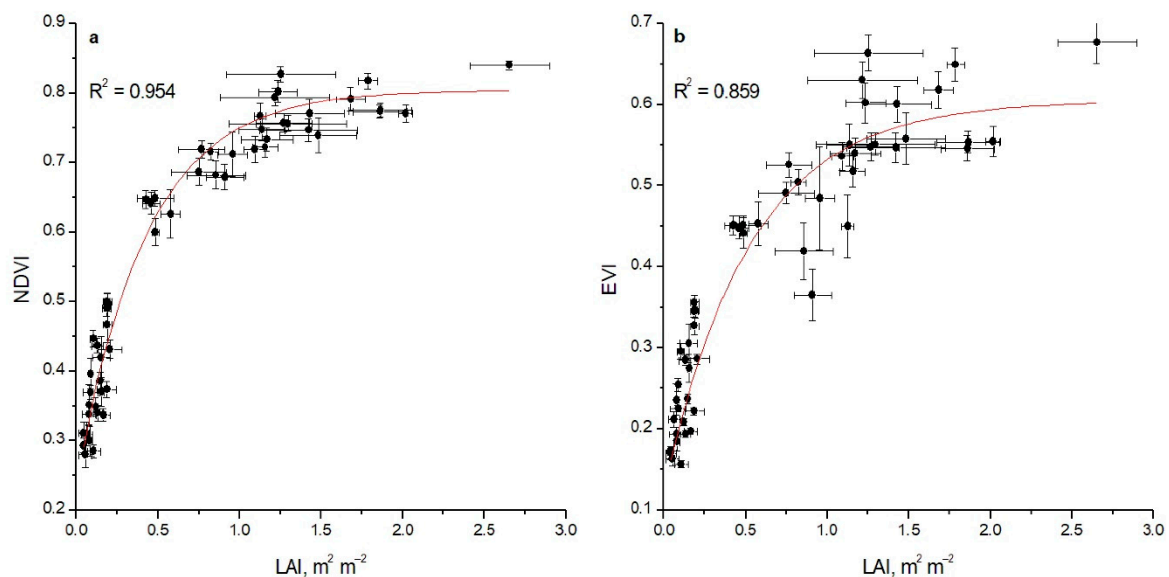


**Figure 6.** Relationships between field-measured LAI and Sentinel-2 NDVI (a) and EVI (b). Data concern dates with both acquisitions and field measurements. Each point corresponds to the mean from three LAI measurements performed in one plot at one date and the mean from the corresponding nine Sentinel-2 pixels  $\pm$  standard deviation.

### 3.1.3. Plant Signal

Vegetation indices incorporating the red part of the spectrum (NDVI and EVI), where chlorophyll absorbs, were used as plant signal. Their performance was examined in the pilot field against final yield maps, resampled, and collocated according to Sentinel-2 spatial resolution ( $10 \times 10$  m), to enable a pixel-to-pixel comparison basis (Figure 2). To that purpose, VI integrals of several time spans as well as single date VIs were compared to final yield data.

Our initial hypothesis was that the whole growing period integral might show lower correlation with yield data compared to the integral for the period from flowering to harvesting, due to the fact that most of the assimilates are directed to seed formation after flowering [43]. Indeed, as shown in Table 2 and Figure 7, there is no correlation between the whole growing period integral (1 December–31 May) and yield (Figure 7a,b) for both NDVI and EVI. On the contrary, strong correlations appear when the integral from flowering to the end of the growing period (20 April–31 May, Figure 7c,d) or the best 20 days integral after the flowering period (6–25 May) are examined. Additionally, especially for NDVI, high correlations also appear when the single date with maximum seasonal value (max NDVI) is considered (Table 2). In all high correlation cases NDVI seems to perform better than EVI. According to the above, only the high correlation cases from each VI are further considered in model configuration.

**Table 2.** Correlation coefficients between final yield and vegetation indices for various integration periods and maximum VI values. Best 20 days integral concerns the 6–25 May period. Data concern the pilot field, corresponding to 221 pixels. Bold numbers denote the highest correlations for each VI.

Integration Period	NDVI	EVI
1 December–31 May	0.047	0.163
20 April–31 May	<b>0.758</b>	<b>0.683</b>
best 20 days	0.719	0.659
max	0.659	0.401

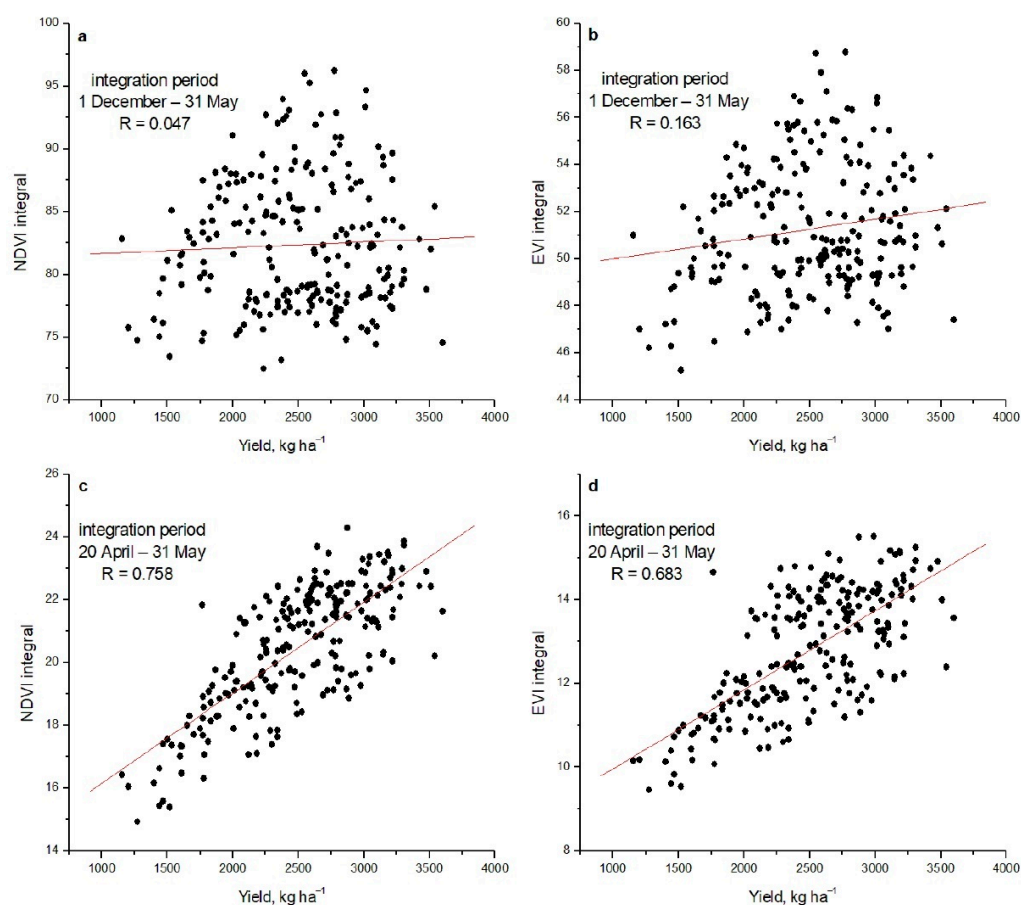


**Figure 7.** Relationships between final yield and VIs for the worst (a,b) and the best (c,d) integration periods. Data concern pilot field, corresponding to 221 pixels.

### 3.1.4. Water Signal

Water potential was measured in the pilot field only during April and May, since at earlier dates plant shoots were too fragile to be inserted intact in the pressure bomb apparatus. As shown in Figure 8, plants showed a good water status during April and gradually lost water during the high temperature/low precipitation May. Noteworthy are the large error bars during the last May measurement, indicating a large in-field variability.

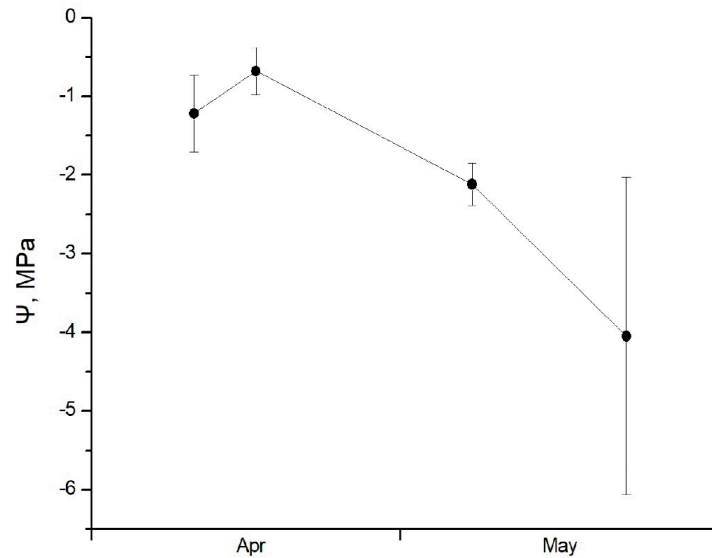


**Figure 8.** Seasonal fluctuation of water potential ( $\Psi$ ). Each point corresponds to the mean from six measurements (one measurement per plot)  $\pm$  standard deviation.

Subsequently, two satellite indices which incorporate water bands (NDWI and NMDI), were examined for their efficiency in depicting the water potential fluctuations. As shown in Figure 9, both indices showed good correlation with water potential. Even though NMDI is generally considered an advantageous water index as it incorporates two water bands, it showed weaker correlation with  $\Psi$  compared to NDWI.

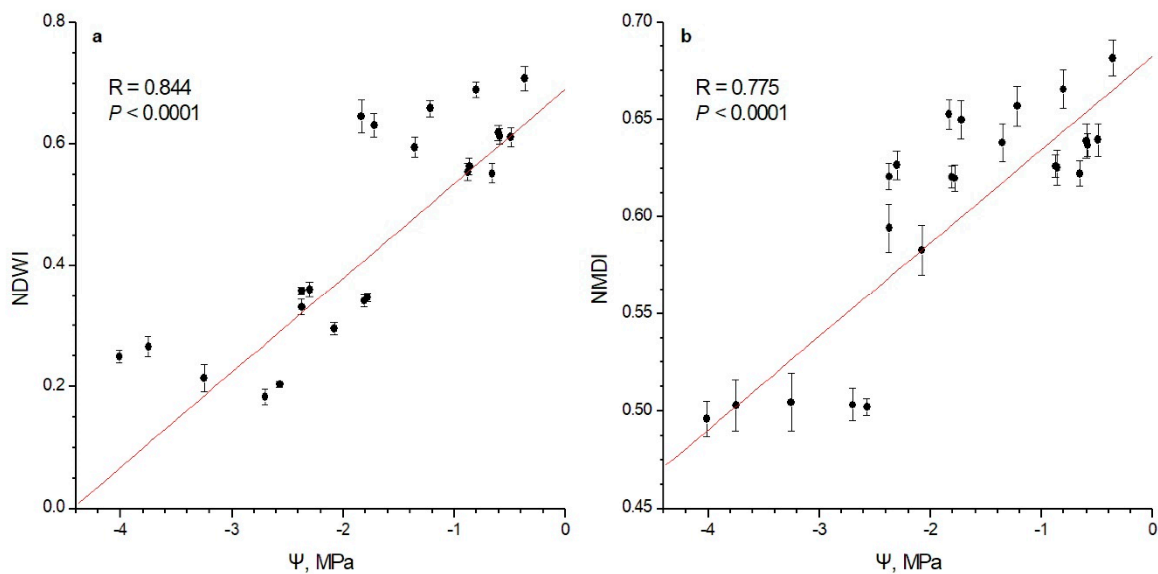


**Figure 9.** Relationships between water potential ( $\Psi$ ) and Sentinel-2 water indices NDWI (a) and NMDI (b). Data concern dates with both Sentinel-2 acquisitions and field measurements. Each point corresponds to one  $\Psi$  measurement performed in one plot at one date and the mean from the corresponding 9 Sentinel-2 pixels  $\pm$  standard deviation.

Accordingly, in order to examine the importance of incorporation of a satellite water signal in the model, the correlation of the two water indices against final yield throughout the growing period were investigated. For both indices the most significant water signal (highest seasonal correlation) was found for 29 April ( $R = 0.641$  and  $0.550$  for NDWI and NMDI, respectively), shortly after flowering. This period is recognized as one of the most crucial for a high final yield of winter wheat [44,45].

### 3.1.5. Soil Signal

As shown in Figure 2d, the pilot field exhibits a particularly wide range of soil ECa values, between  $30$  and  $130 \text{ mS m}^{-1}$ , which is expected to affect final yield production [46,47]. Indeed, as shown in Figure 10, final yield is highly correlated with soil ECa; higher productivity occurs in areas of lower ECa and vice versa. In an attempt to depict this soil variability through a remote-sensed soil signal, the correlations of Sentinel-2 bands (reflectance) as well as several indices from a single date before the crop establishment (i.e., during bare ground period) were examined against ECa and final yield. As shown in Table 1, among Sentinel-2 bands, band 12 exhibits the highest correlation with ECa, followed by band 11. This result may be ascribed to the fact that both bands incorporate water signals. Accordingly, NMDI—incorporating both 11 and 12 bands—shows the highest correlation with soil conductivity, followed by NDWI which incorporates only band 12. However, it is worth to note that NDVI of bare ground also shows a high correlation with ECa.

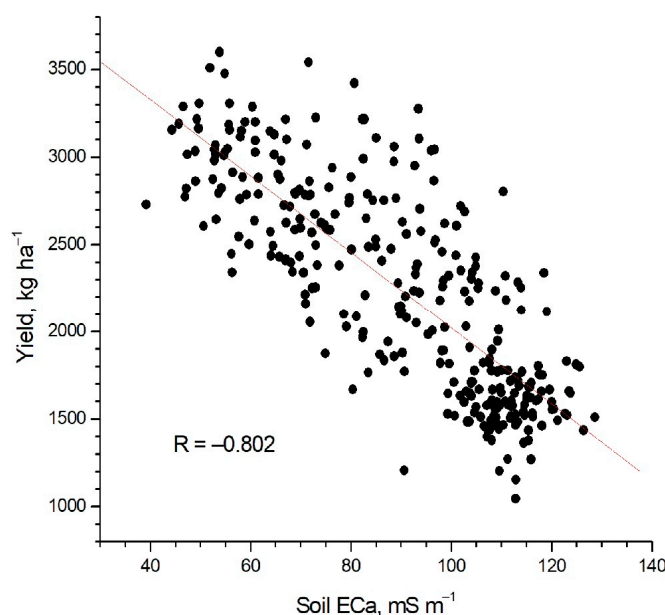


**Figure 10.** Relationship between soil ECa and final yield.

### 3.2. Model Configuration

The combination of the components described above, i.e., plant, water, and soil signals, was examined against final yield by multilinear regression analysis in the pilot field. Several combinations of VIs corresponding to the three signals were tested and are presented in Table 3. More specifically, concerning plant signal, NDVI and EVI integrals from flowering to the end of the growing period (20 April–31 May) or the best 20 days period after flowering (6–25 May) and their maximum seasonal value (max) were examined. Accordingly, for water signal, NDWI and NMDI for the date with the maximum correlation with final yield (29 April), i.e., the most critical water period, were incorporated. Finally, NDWI and NMDI for a single date before sowing were tested as soil signals.

As shown in Table 3, the best final yield estimation is achieved by a model version combining the NDVI integral from 20 April to 31 May as plant signal, NDWI at 29 April as water signal, and NDWI of bare ground as soil signal (Figure 11a). However, model

versions with NMDI as water and/or soil signals show similar high correlations with final yield. For EVI used as plant signal, the best estimation of final yield was also achieved by the 20 April–31 May integral. It is also noteworthy that the performance of a model version with a single date NDVI (Max) for all water and soil signal combinations, was remarkably high further extending the potential for early season yield prediction.

**Table 3.** Coefficients of determination ( $R^2$ ) and root mean square error (RMSE,  $\text{kg ha}^{-1}$ ) between measured final yield and various model versions incorporating different plant, water, and soil signals. Best 20 days integral concerns the 6–25 May period. Data concern the pilot field, corresponding to 221 pixels. The most significant correlations are indicated in bold.

Plant Signal			NDVI		EVI	
Integration Period	Water Signal	Soil Signal	$R^2$	RMSE	$R^2$	RMSE
20 April–31 May	NMDI	NMDI	0.584	334	0.484	371
20 April–31 May	NMDI	NDWI	0.607	325	0.542	351
20 April–31 May	NDWI	NMDI	0.604	326	0.484	371
20 April–31 May	NDWI	NDWI	<b>0.619</b>	<b>319</b>	<b>0.542</b>	<b>350</b>
Best 20 days	NMDI	NMDI	0.526	357	0.457	381
Best 20 days	NMDI	NDWI	0.549	348	0.504	364
Best 20 days	NDWI	NMDI	0.526	357	0.462	380
Best 20 days	NDWI	NDWI	0.549	348	0.508	363
Max	NMDI	NMDI	0.460	381	0.328	424
Max	NMDI	NDWI	0.483	372	0.364	413
Max	NDWI	NMDI	0.462	380	0.442	387
Max	NDWI	NDWI	0.491	369	0.468	378

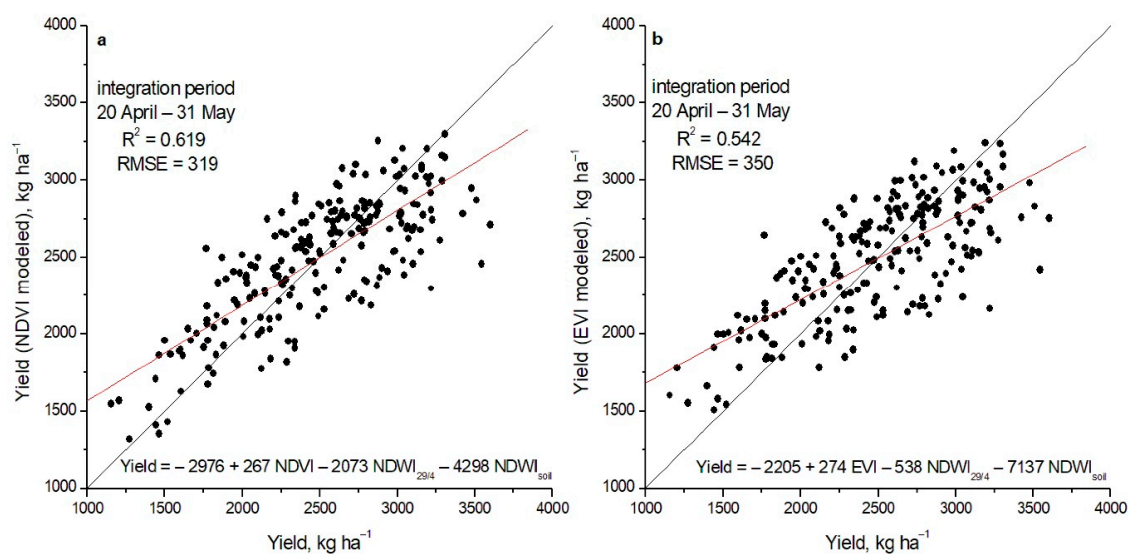


**Figure 11.** Relationships between measured yield and best model estimates based on NDVI (a) or EVI (b) as plant signal. For both models, water and soil signals correspond to NDWI on 29 April and NDWI before sowing, respectively. Data concern the pilot field, corresponding to 221 pixels. The black line corresponds to the 1:1 line and the red is the best-fit line. The equations of the modelled yield obtained from the multiple linear regressions are indicated in the graphs.

### 3.3. Model Extension/Evaluation

In order to extend/evaluate the models described in the previous step for the pilot field, their versions were tested in 31 fields during the 2017–2018 and 2018–2019 growing periods, with a total number of 7436 pixels. It has to be noted that the pilot field was a low productivity field with a yield range between 1000 and 3500  $\text{kg ha}^{-1}$ , whereas the 31 fields used in the extension/evaluation step covered a yield range from 2000 to 7500  $\text{kg ha}^{-1}$ . Accordingly, the full equations determined through multiple linear regression analysis in the pilot field were not used per se in the 31 fields, but only the same signal parameters

determined previously were used in a new regression analysis. Therefore, in this step, evaluation concerns the use of the same signal parameters, while extension concerns the new multilinear regressions with these parameters.

As shown in Table 4, the best-performing versions of the model concern the same plant signals as in the previous step (NDVI and EVI integrals for the 20 April–31 May period), but NMDI instead of NDWI as water and soil signals ( $R^2 = 0.613$ , RMSE = 549 for NDVI and  $R^2 = 0.629$ , RMSE = 538 for EVI, Figure 12). However, in contrast to the previous step where NDVI was found to perform better than EVI as plant signal, in this step EVI performed better, even though the differences from NDVI were marginal. Accordingly, the performance of the model version with maximum VI as plant signal (max) was very good ( $R^2 = 0.584$ , RMSE = 570 for NDVI and  $R^2 = 0.587$ , RMSE = 568 for EVI), corroborating its applicability for early and simple yield predictions.

**Table 4.** Coefficients of determination ( $R^2$ ) and root mean square error (RMSE,  $\text{kg ha}^{-1}$ ) between measured final yield and various model versions incorporating different plant, water, and soil signals. Best 20 days integral concerns the 13 April–2 May period. Data concern 31 fields during two growing periods, corresponding to 7436 pixels. The most significant correlations are indicated in bold.

Plant Signal			NDVI		EVI	
Integration Period	Water Signal	Soil Signal	$R^2$	RMSE	$R^2$	RMSE
20 April–31 May	NMDI	NMDI	<b>0.613</b>	<b>549</b>	<b>0.629</b>	<b>538</b>
20 April–31 May	NMDI	NDWI	0.604	556	0.619	545
20 April–31 May	NDWI	NMDI	0.542	598	0.566	582
20 April–31 May	NDWI	NDWI	0.551	591	0.572	579
Best 20 days	NMDI	NMDI	0.587	567	0.598	560
Best 20 days	NMDI	NDWI	0.578	574	0.587	568
Best 20 days	NDWI	NMDI	0.523	610	0.542	598
Best 20 days	NDWI	NDWI	0.530	606	0.542	597
Max	NMDI	NMDI	0.584	570	0.587	568
Max	NMDI	NDWI	0.572	578	0.570	579
Max	NDWI	NMDI	0.520	612	0.521	611
Max	NDWI	NDWI	0.523	610	0.521	611

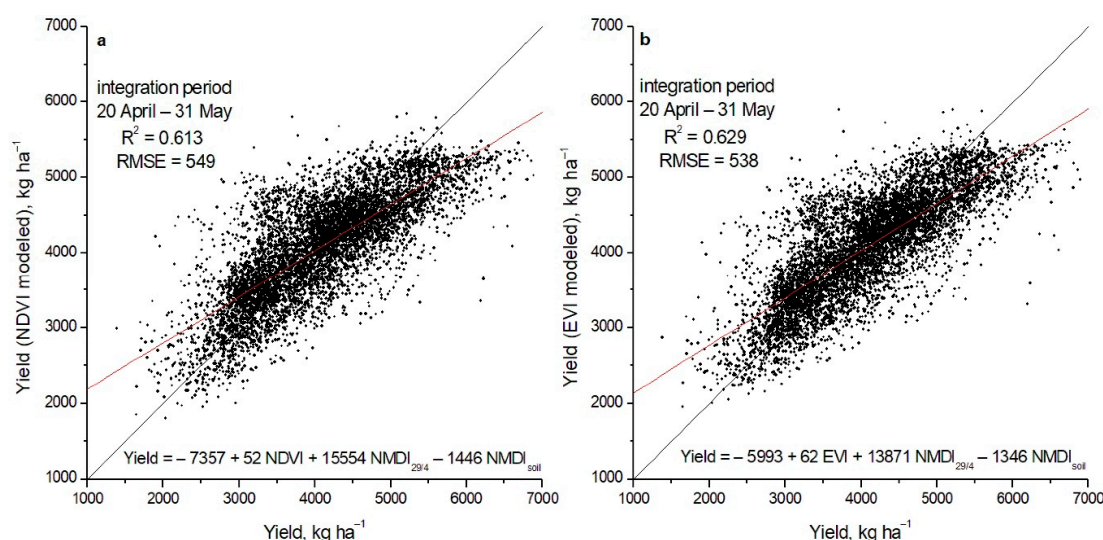


**Figure 12.** Relationships between measured yield and best model estimates based on NDVI (a) or EVI (b) as plant signal. For both models, water and soil signals correspond to NDWI on 29 April and NDWI before sowing accordingly. Data concern 31 fields during two growing periods, corresponding to 7436 pixels. The black line corresponds to the 1:1 line and the red is the best-fit line. The equations of the modelled yield obtained from the multiple linear regressions are indicated in the graphs.

## 4. Discussion

### 4.1. Plant, Water, and Soil Signals

In this study, a two-step process for the development of a single model for wheat yield prediction based on Sentinel-2 satellite data was followed. The determination of the satellite-derived parameters used in the modelling process was based on field ecophysiological measurements performed in a pilot field. The plant signals obtained from NDVI and EVI showed a high correlation with the field-measured canopy reflectance. Sentinel-2 performance was evaluated on the basis of VIs intercomparisons with the hyperspectral JAZ canopy spectroradiometer of 0.3 nm spectral analysis, which operated very close to the canopy avoiding any atmospheric disturbance effects (Figure 3). Additionally, both NDVI and EVI well depicted the seasonal development of the winter wheat crop (Figure 5). Durum wheat in south Europe is planted in late autumn, usually during November or December, seedlings emerge shortly after, and tillering is completed during the winter period. Flowering is considered a critical period of the crop [48,49] and usually occurs in the middle of April in the Thessaly plain. This growth profile was closely followed by both field-measured LAI and satellite VIs, which showed low values during winter, gradually increasing until April flowering period, followed by a rather steep decrease during May seed-ripening period.

In order to identify the optimum period for predicting potential yield, the daily VI data produced by a timeseries interpolation process for each Sentinel-2 pixel were examined against yield maps recorded by the harvester. The results showed that for both NDVI and EVI virtually no correlation was found between the whole growing period integral (1 December–31 May) and yield, while strong correlations appeared when the integral from flowering to the end of the growing period, or the best 20 days integral after the flowering period, was taken into account (Figure 7). During this particular period, plants start to lose their chlorophylls [50], so VIs were declining (Figure 5). For the Mediterranean region, this period is considered crucial in determining the final yield because the plants direct their photosynthetic products to the seed [2,49]. The results are in contrast with findings from Ren et al. [22] and Becker-Reshef et al. [9] who declared that the best correlation between NDVI and wheat yield coincides with the period of highest LAI achieved a few days before flowering. However, corroborating our results, Lopresti et al. [24] reported that prediction of wheat yield is best 30 days before harvest, after the stages of heading and flowering. Seggara et al. [51] investigated the optimum period for winter wheat yield estimation in Spain and found that the predictions made on the heading stage outperformed the predictions on tillering or maturing stages, but they did not make any observations during the stage of flowering.

The water signal incorporated in our model was derived from two satellite water indices (NDWI, NMDI), whose efficiency to monitor variations in plant water content was examined by comparing them with field-measured plant water potential. Although NMDI is considered more advantageous compared to NDWI as it incorporates two water bands, it showed a weaker correlation with  $\Psi$  ( $R = 0.775$  vs.  $R = 0.844$ , respectively, Figure 9). Accordingly, NDWI performed better than NMDI as a water signal in the pilot field, but NMDI outperformed NDWI in the application of the model in the second modelling step involving 31 fields during two growing periods, i.e., covering a wider range of conditions.

Soil signal is critical in the construction of a yield prediction model, especially in the case of remarkably variable soil properties, such as ECa. The pilot field of the present study displayed a particularly high range of soil ECa between 30 and 130  $\text{mS m}^{-1}$ , which showed a strong negative linear relationship with wheat yield (Figure 10). Therefore, to address the challenge of capturing such a wide range of ECa through remote-sensed data, the correlations of Sentinel-2 bands and several indices from a single date before the crop establishment (i.e., during bare ground period) were examined against ECa and final yield. NDWI and NMDI of bare ground presented high correlations and were selected for further testing in the procedure of model development. As in the case of the water signal, NDWI

performed better than NMDI in the pilot field, and NMDI better in the 31 fields step, indicating its superiority for wide range conditions applications.

#### 4.2. Model Development and Validation

Yield prediction of durum wheat has been of major interest both from an economical and managerial point of view. Its accurate prediction requires identification of crop variability even at a within-field scale [8]. The development of remote sensing technologies based mainly on satellite observations made possible the assessment of within-field variability. The Sentinel-2 satellites, operated by the ESA Copernicus program, introduced a new era in open source, high spatial resolution, and frequent earth observations. This advancement is promising not only for capturing within-field variability but also for monitoring of small-sized fields. The latter is crucial for arable lands of the Mediterranean basin due to the small area of farms, the monitoring of which requires high spatial resolution of the remotely sensed data.

The evolution of yield prediction models started with laborious ecophysiological measurements-based simulations and continued with the first generation of satellite-based measurements incorporating low resolution data. During the last decade, complex models have been proposed that require numerous inputs such as soil properties, crop variety information, and meteorological data. Quite often though, the availability or the accessibility of such a broad information is limited. Therefore, there is an essential need for the construction of prediction models that are minimal in inputs and incorporate variables which are easily accessed. In countries like Greece, for example, meteorological data of arable land are not always available or easily accessible. Additionally, between-years climate fluctuation may be unpredictable in the Mediterranean region, especially in the framework of the ongoing climate change. Thus, finding the balance between simplicity and accuracy may result in advantageous next-generation models, with the following characteristics: (i) have as few as possible inputs, without compromising accuracy, (ii) preferentially use satellite data which are easily accessible and present a good correlation with plant function and productivity, (iii) efficiently fit to small farms but could be extended to cover a range of similar environments and cultivation years—high spatial and temporal analysis and extension. In line with this, satellite-based models which utilize the VIs provided by new generation satellites, like ESA's Sentinel-2, are expected to be proved valuable, as they provide information of high spatial and temporal scales.

The modeling procedure presented in this study aimed at addressing the above-mentioned needs. The satellite-derived parameters corresponding to plant, water, and soil signals that were determined in the pilot field were further extended/evaluated on 31 other durum wheat fields located in the Thessaly plain throughout two different cultivation years. As shown in Figures 7 and 12, the pilot field was a low-productivity field (yield between 1000 and 3500 kg ha<sup>-1</sup>), whereas the numerous fields used in the extension/evaluation procedure covered a much wider yield range (2000 to 7500 kg ha<sup>-1</sup>). Accordingly, the models developed in the pilot field were not used per se in the other fields, but new regressions with the same signal parameters determined previously were made. Our results show that the overall best performing model version involves the EVI integral for the 20 April–31 May period as a plant signal and NMDI at 29 April and before sowing as water and soil signals, respectively ( $R^2 = 0.629$ , RMSE = 538). This model version may be used for yield estimation but not for yield prediction since it incorporates data until the end of the growing period. However, as has been shown (Table 4), the model versions with the maximum seasonal VIs values as plant signal performed almost equally well; the best-performing version involved the max EVI as plant signal and NMDI as water and soil signals ( $R^2 = 0.587$ , RMSE = 568). Usually, the maximum seasonal VIs values are recorded during the last ten days of April (Figure 5), i.e., 30 to 50 days in advance before harvest. Additionally, for this model version only one satellite image is needed for the estimation of the plant signal parameter, significantly simplifying the application of the model.

Future work will focus on the optimization of the proposed model through incorporation of additional fields with different soil characteristics and management practices and/or in different areas and cultivation years. Thus, by increasing the conditions range, the equations determined by multilinear regression analysis are expected to become fine-tuned leading finally to a robust widely applied model. To this end, the determination of the significant signal parameters involved in the modeling approach, which was made in this study, is the first step of the process. Even if it is proved that this approach cannot be applied for widely different conditions, model parameterization for relatively small areas with similar conditions will be a rather simple process. Additionally, the estimation/prediction accuracy of the models presented in this study may be further enhanced if they are used as the basis in productivity models like the ones following the light use efficiency approach, which may better account for climatic and regional variability, increasing however the complexity of the process.

## 5. Conclusions

The high spatial and temporal resolution of VIs retrieved from Sentinel-2 imagery enabled the development of several models for durum wheat yield estimation/prediction with good accuracy. EVI was found to function marginally better from NDVI as a plant signal, while NMDI outperformed NDWI as water and soil signals. The best performing model version for yield estimation involved the EVI integral for the 20 April–31 May period as a plant signal and NMDI at 29 April and before sowing as water and soil signals, respectively ( $R^2 = 0.629$ , RMSE = 538). Accordingly, the best performing single date model for yield prediction was attained by a version involving the seasonal max EVI as plant signal and NMDI as water and soil signals ( $R^2 = 0.587$ , RMSE = 568) 30 to 50 days in advance before harvest. The main advantages of the presented model are its simplicity, the use of easily accessible satellite data of high spatial resolution, and its accuracy in small farms of the Thessaly plain, as was proved in the validation process. Therefore, this durum wheat yield prediction model can be a useful tool for stakeholders, especially dealers, traders, and pasta food companies.

**Author Contributions:** Conceptualization, C.C. and A.K.; investigation, C.C., S.M., M.M., K.A., M.S., E.L. and A.K.; writing—original draft preparation, C.C. and A.K.; writing—review and editing, C.C., E.L. and A.K. All authors have read and agreed to the published version of the manuscript.

**Funding:** This research was partially funded by Barilla Hellas S.A. for the pilot field measurements.

**Acknowledgments:** The authors would like to thank Alfa Seeds Ltd (Larisa, Greece) for kindly providing the yield data from the combine harvester used in the present study.

**Conflicts of Interest:** The authors declare no conflict of interest. The funders had no role in the design of the study; in the collection, analyses, or interpretation of data; in the writing of the manuscript, or in the decision to publish the results.

## References

1. Royo, C.; Soriano, J.M.; Alvaro, F. *Wheat: A Crop in the Bottom of the Mediterranean Diet Pyramid*; IntechOpen: London, UK, 2017; ISBN 978-953-51-3586-9.
2. Diacono, M.; Castrignanò, A.; Troccoli, A.; De Benedetto, D.; Basso, B.; Rubino, P. Spatial and Temporal Variability of Wheat Grain Yield and Quality in a Mediterranean Environment: A Multivariate Geostatistical Approach. *Field Crops Res.* **2012**, *131*, 49–62. [[CrossRef](#)]
3. Ritchie, J.; Otter, S. Description and Performance of CERES-Wheat: A User-Oriented Wheat Yield Model. *USDA-ARS* **1985**, *38*, 159–175.
4. Van Diepen, C.A.; Wolf, J.; van Keulen, H.; Rappoldt, C. WOFOST: A Simulation Model of Crop Production. *Soil Use Manag.* **1989**, *5*, 16–24. [[CrossRef](#)]
5. Evert, F.K.V.; Campbell, G.S. CropSyst: A Collection of Object-Oriented Simulation Models of Agricultural Systems. *Agron. J.* **1994**, *86*, 325–331. [[CrossRef](#)]
6. Duchemin, B.; Maisongrande, P.; Boulet, G.; Benhadj, I. A Simple Algorithm for Yield Estimates: Evaluation for Semi-Arid Irrigated Winter Wheat Monitored with Green Leaf Area Index. *Environ. Model. Softw.* **2008**, *23*, 876–892. [[CrossRef](#)]

7. Basso, B.; Liu, L.; Ritchie, J.T. A Comprehensive Review of the CERES-Wheat, -Maize and -Rice Models' Performances. In *Advances in Agronomy*; Sparks, D.L., Ed.; Advances in Agronomy; Academic Press: Cambridge, MA, USA, 2016; Volume 136, pp. 27–132.
8. Wiegand, C.L.; Richardson, A.J. Use of Spectral Vegetation Indices to Infer Leaf Area, Evapotranspiration and Yield: I. Rationale. *Agron. J.* **1990**, *82*, 623–629. [[CrossRef](#)]
9. Becker-Reshef, I.; Vermote, E.; Lindeman, M.; Justice, C. A Generalized Regression-Based Model for Forecasting Winter Wheat Yields in Kansas and Ukraine Using MODIS Data. *Remote Sens. Environ.* **2010**, *114*, 1312–1323. [[CrossRef](#)]
10. Padilla, F.L.M.; Maas, S.J.; González-Dugo, M.P.; Mansilla, F.; Rajan, N.; Gavilán, P.; Domínguez, J. Monitoring Regional Wheat Yield in Southern Spain Using the GRAMI Model and Satellite Imagery. *Field Crops Res.* **2012**, *130*, 145–154. [[CrossRef](#)]
11. Silvestro, P.C.; Pignatti, S.; Pascucci, S.; Yang, H.; Li, Z.; Yang, G.; Huang, W.; Casa, R. Estimating Wheat Yield in China at the Field and District Scale from the Assimilation of Satellite Data into the Aquacrop and Simple Algorithm for Yield (SAFY) Models. *Remote Sens.* **2017**, *9*, 509. [[CrossRef](#)]
12. Gaso, D.V.; Berger, A.G.; Ciganda, V.S. Predicting Wheat Grain Yield and Spatial Variability at Field Scale Using a Simple Regression or a Crop Model in Conjunction with Landsat Images. *Comput. Electron. Agric.* **2019**, *159*, 75–83. [[CrossRef](#)]
13. Rouse, J.W., Jr.; Haas, R.H.; Schell, J.A.; Deering, D.W. Monitoring Vegetation Systems in the Great Plains with Erts. *NASA Spec. Publ.* **1974**, *351*, 309.
14. Huete, A.; Didan, K.; Miura, T.; Rodriguez, E.P.; Gao, X.; Ferreira, L.G. Overview of the Radiometric and Biophysical Performance of the MODIS Vegetation Indices. *Remote Sens. Environ.* **2002**, *83*, 195–213. [[CrossRef](#)]
15. Barnes, E.M.; Clarke, T.R.; Richards, S.E.; Colaizzi, P.D.; Haberland, J.; Kostrzewski, M.; Waller, P.; Choi, C.; Riley, E.; Thompson, T. Coincident Detection of Crop Water Stress, Nitrogen Status and Canopy Density Using Ground-Based Multispectral Data. In Proceedings of the 5th International Conference on Precision Agriculture, Bloomington, MN, USA, 16–19 July 2000.
16. Prince, S.D. A Model of Regional Primary Production for Use with Coarse Resolution Satellite Data. *Int. J. Remote Sens.* **1991**, *12*, 1313–1330. [[CrossRef](#)]
17. Baret, F.; Guyot, G. Potentials and Limits of Vegetation Indices for LAI and APAR Assessment. *Remote Sens. Environ.* **1991**, *35*, 161–173. [[CrossRef](#)]
18. Johnen, T.; Boettcher, U.; Kage, H. An Analysis of Factors Determining Spatial Variable Grain Yield of Winter Wheat. *Eur. J. Agron.* **2014**, *52*, 297–306. [[CrossRef](#)]
19. Satir, O.; Berberoglu, S. Crop Yield Prediction under Soil Salinity Using Satellite Derived Vegetation Indices. *Field Crops Res.* **2016**, *192*, 134–143. [[CrossRef](#)]
20. Wall, L.; Larocque, D.; Léger, P.-M. The Early Explanatory Power of NDVI in Crop Yield Modelling. *Int. J. Remote Sens.* **2008**, *29*, 2211–2225. [[CrossRef](#)]
21. Balaghi, R.; Tychon, B.; Eerens, H.; Jlibene, M. Empirical Regression Models Using NDVI, Rainfall and Temperature Data for the Early Prediction of Wheat Grain Yields in Morocco. *Int. J. Appl. Earth Obs. Geoinf.* **2008**, *10*, 438–452. [[CrossRef](#)]
22. Ren, J.; Chen, Z.; Zhou, Q.; Tang, H. Regional Yield Estimation for Winter Wheat with MODIS-NDVI Data in Shandong, China. *Int. J. Appl. Earth Obs. Geoinf.* **2008**, *10*, 403–413. [[CrossRef](#)]
23. Bolton, D.K.; Friedl, M.A. Forecasting Crop Yield Using Remotely Sensed Vegetation Indices and Crop Phenology Metrics. *Agric. For. Meteorol.* **2013**, *173*, 74–84. [[CrossRef](#)]
24. Lopresti, M.F.; Di Bella, C.M.; Degioanni, A.J. Relationship between MODIS-NDVI Data and Wheat Yield: A Case Study in Northern Buenos Aires Province, Argentina. *Inf. Process. Agric.* **2015**, *2*, 73–84. [[CrossRef](#)]
25. Nagy, A.; Fehér, J.; Tamás, J. Wheat and Maize Yield Forecasting for the Tisza River Catchment Using MODIS NDVI Time Series and Reported Crop Statistics. *Comput. Electron. Agric.* **2018**, *151*, 41–49. [[CrossRef](#)]
26. Prey, L.; Schmidhalter, U. Simulation of Satellite Reflectance Data Using High-Frequency Ground Based Hyperspectral Canopy Measurements for in-Season Estimation of Grain Yield and Grain Nitrogen Status in Winter Wheat. *ISPRS J. Photogramm. Remote Sens.* **2019**, *149*, 176–187. [[CrossRef](#)]
27. Moriondo, M.; Maselli, F.; Bindi, M. A Simple Model of Regional Wheat Yield Based on NDVI Data. *Eur. J. Agron.* **2007**, *26*, 266–274. [[CrossRef](#)]
28. Bhattacharya, B.K.; Mallick, K.; Nigam, R.; Dakore, K.; Shekh, A.M. Efficiency Based Wheat Yield Prediction in a Semi-Arid Climate Using Surface Energy Budgeting with Satellite Observations. *Agric. For. Meteorol.* **2011**, *151*, 1394–1408. [[CrossRef](#)]
29. Hatfield, J.L. Remote Sensing Estimators of Potential and Actual Crop Yield. *Remote Sens. Environ.* **1983**, *13*, 301–311. [[CrossRef](#)]
30. Quarmby, N.A.; Milnes, M.; Hindle, T.L.; Silleos, N. The Use of Multi-Temporal NDVI Measurements from AVHRR Data for Crop Yield Estimation and Prediction. *Int. J. Remote Sens.* **1993**, *14*, 199–210. [[CrossRef](#)]
31. Hayes, M.J.; Decker, W.L. Using NOAA AVHRR Data to Estimate Maize Production in the United States Corn Belt. *Int. J. Remote Sens.* **1996**, *17*, 3189–3200. [[CrossRef](#)]
32. Labus, M.P.; Nielsen, G.A.; Lawrence, R.L.; Engel, R.; Long, D.S. Wheat Yield Estimates Using Multi-Temporal NDVI Satellite Imagery. *Int. J. Remote Sens.* **2002**, *23*, 4169–4180. [[CrossRef](#)]
33. Mika, J.; Kerényi, J.; Rimóczi-Paál, A.; Merza, Á.; Szinell, C.; Csiszár, I. On Correlation of Maize and Wheat Yield with NDVI: Example of Hungary (1985–1998). *Adv. Space Res.* **2002**, *30*, 2399–2404. [[CrossRef](#)]
34. Kastens, J.H.; Kastens, T.L.; Kastens, D.L.A.; Price, K.P.; Martinko, E.A.; Lee, R.-Y. Image Masking for Crop Yield Forecasting Using AVHRR NDVI Time Series Imagery. *Remote Sens. Environ.* **2005**, *99*, 341–356. [[CrossRef](#)]

35. Salazar, L.; Kogan, F.; Roytman, L. Use of Remote Sensing Data for Estimation of Winter Wheat Yield in the United States. *Int. J. Remote Sens.* **2007**, *28*, 3795–3811. [CrossRef]
36. User Guides—Sentinel Online—Sentinel. Available online: <https://sentinel.esa.int/web/sentinel/user-guides> (accessed on 24 June 2021).
37. Xie, Q.; Dash, J.; Huete, A.; Jiang, A.; Yin, G.; Ding, Y.; Peng, D.; Hall, C.C.; Brown, L.; Shi, Y.; et al. Retrieval of Crop Biophysical Parameters from Sentinel-2 Remote Sensing Imagery. *Int. J. Appl. Earth Obs. Geoinf.* **2019**, *80*, 187–195. [CrossRef]
38. Norman, J.M.; Jarvis, P.G. Photosynthesis in Sitka Spruce (*Picea Sitchensis* (Bong.) Carr.). III. Measurements of Canopy Structure and Interception of Radiation. *J. Appl. Ecol.* **1974**, *11*, 375–398. [CrossRef]
39. Sudduth, K.; Drummond, S.T.; Myers, D. Yield Editor 2.0: Software for Automated Removal of Yield Map Errors. In Proceedings of the ASABE Annual International Meeting, Dallas, TX, USA, 29 July–1 August 2012; Volume 4.
40. Open Access Hub. Available online: <https://scihub.copernicus.eu/> (accessed on 1 September 2019).
41. European Space Agency. STEP—Science Toolbox Exploitation Platform. Available online: <http://step.esa.int> (accessed on 1 September 2019).
42. JASP—A Fresh Way to Do Statistics. Available online: <https://jasp-stats.org/> (accessed on 28 June 2021).
43. Gonzalez-Navarro, O.E.; Griffiths, S.; Molero, G.; Reynolds, M.P.; Slafer, G.A. Variation in Developmental Patterns among Elite Wheat Lines and Relationships with Yield, Yield Components and Spike Fertility. *Field Crops Res.* **2016**, *196*, 294–304. [CrossRef] [PubMed]
44. Zhang, H.; Wang, X.; You, M.; Liu, C. Water-Yield Relations and Water-Use Efficiency of Winter Wheat in the North China Plain. *Irrig. Sci.* **1999**, *19*, 37–45. [CrossRef]
45. Wu, J.; Liu, M.; Lü, A.; He, B. The Variation of the Water Deficit during the Winter Wheat Growing Season and Its Impact on Crop Yield in the North China Plain. *Int. J. Biometeorol.* **2014**, *58*, 1951–1960. [CrossRef]
46. Sun, Y.; Druecker, H.; Hartung, E.; Hueging, H.; Cheng, Q.; Zeng, Q.; Sheng, W.; Lin, J.; Roller, O.; Paetzold, S.; et al. Map-Based Investigation of Soil Physical Conditions and Crop Yield Using Diverse Sensor Techniques. *Soil Tillage Res.* **2011**, *112*, 149–158. [CrossRef]
47. Yang, W.; Li, M.; Zheng, L.; Sun, H. Evaluation Model of Winter Wheat Yield Based on Soil Properties. In *Computer and Computing Technologies in Agriculture VIII*; IFIP Advances in Information and Communication Technology; Li, D., Chen, Y., Eds.; Springer International Publishing: Cham, Switzerland, 2015; Volume 452, pp. 638–645. ISBN 978-3-319-19619-0.
48. Aparicio, N.; Villegas, D.; Araus, J.L.; Casadesús, J.; Royo, C. Relationship between Growth Traits and Spectral Vegetation Indices in Durum Wheat. *Crop Sci.* **2002**, *42*, 1547–1555. [CrossRef]
49. Cossani, C.M.; Slafer, G.A.; Savin, R. Yield and Biomass in Wheat and Barley under a Range of Conditions in a Mediterranean Site. *Field Crops Res.* **2009**, *112*, 205–213. [CrossRef]
50. Islam, M.; Haque, K.M.; Akter, N.; Karim, M. Leaf Chlorophyll Dynamics in Wheat Based on SPAD Meter Reading and Its Relationship with Grain Yield. *Sci. Agric.* **2014**, *4*, 13–18. [CrossRef]
51. Segarra, J.; González-Torralla, J.; Aranjuelo, Í.; Araus, J.L.; Kefauver, S.C. Estimating Wheat Grain Yield Using Sentinel-2 Imagery and Exploring Topographic Features and Rainfall Effects on Wheat Performance in Navarre, Spain. *Remote Sens.* **2020**, *12*, 2278. [CrossRef]